Light-trapping design for thin-film silicon-perovskite tandem solar cells

Stephen Foster and Sajeev John

Light-trapping design for thin-film silicon-perovskite tandem solar cells

Stephen Foster[a)] and Sajeev John
Department of Physics, University of Toronto, Toronto, Ontario M5S1A7, Canada

Using finite-difference time-domain simulations, we investigate the optical properties of tandem silicon/perovskite solar cells with a photonic crystal architecture, consisting of a square-lattice array of inverted pyramids with a center-to-center spacing of 2.5 μm. We demonstrate that near-perfect light-trapping and absorption can be achieved over the 300–1100 nm wavelength range with this architecture, using less than 10 μm (equivalent bulk thickness) of crystalline silicon. Using a one-diode model, we obtain projected efficiencies of over 30% for the two-terminal tandem cell under a current-matching condition, well beyond the current record for single-junction silicon solar cells. The architecture is amenable to mass fabrication through wet-etching and uses a fraction of the silicon of traditional designs, making it an attractive alternative to other silicon-perovskite tandem designs. *Published by AIP Publishing.* [http://dx.doi.org/10.1063/1.4962458]

I. INTRODUCTION

Crystalline silicon (c-Si) solar cells currently dominate the photovoltaic market, with a market share of over 90%.[1] The world record efficiency for c-Si cells has now reached 25.6%,[2] which is already approaching the theoretical limit of 29.4%.[3] However, in order for solar power to be competitive with fossil fuels and other alternative forms of energy, cells with even higher efficiencies will be needed.

One approach to achieving efficiencies beyond the traditional Shockley-Queisser limit is to switch to multi-junction tandem cells, which are capable of making more effective use of the solar spectrum. To date, tandem cells have fallen into two categories: (1) high-efficiency, high-cost triple-junction cells, which are suitable only for space applications or for areas with high direct solar illumination (typically coupled with solar concentrators);[4] and (2) low-cost, low-efficiency cells based on emerging "third-generation" solar cell technologies. Examples in this second category include polymer solar cells,[5,6] dye-sensitized solar cells,[7] quantum-dot solar cells,[8] and hybrid designs such as polymer/quantum-dot[9] and polymer/silicon cells.[10] As of yet, none of these emerging tandem designs have been able to exceed the efficiency of single-junction c-Si cells, but such cells may be able to carve out a market niche given low enough costs. However, in order to displace c-Si cells, a true low-cost, high-efficiency tandem cell is needed.

In recent years, CH$_3$NH$_3$PbI$_3$ perovskite solar cells have made rapid efficiency gains and attracted widespread interest due to their excellent optical and electrical properties and potential low cost.[11] The record efficiency for single-junction perovskite cells is quickly growing and currently stands at 21.0%,[12] by far the highest among emerging solar cell technologies. Projections put the ultimate efficiency limit at roughly 30%, similar to c-Si.[13] This high efficiency, combined with the high absorption coefficient and relatively large bandgap (1.57 eV) of CH$_3$NH$_3$PbI$_3$, makes perovskite cells an attractive

candidate for the top cell in a c-Si-based tandem. For a two-junction tandem with a c-Si bottom cell (bandgap of 1.12 eV), the ideal bandgap for the top cell is 1.75 eV.[14] Although lower than this ideal value, the bandgap of CH$_3$NH$_3$PbI$_3$ is still large enough to produce significant efficiency gains over single-junction c-Si cells. Moreover, the bandgap of CH$_3$NH$_3$PbI$_3$ can be chemically tuned by substituting halogens such as bromine in place of iodine atoms.[15] There are already several examples of perovskite/c-Si tandem cells in the literature,[15–17] with one recent paper demonstrating the potential for efficiencies of 25%.[15]

Another promising avenue to improving solar cell efficiencies is through the use of photonic crystal architectures. Photonic crystals are periodic structures which can provide powerful light trapping effects through resonant scattering and wave interference.[18,19] Coherent illumination is not required for these effects to be observed, giving photonic crystals the capability to trap incoherent sunlight. It has been shown that certain photonic crystal designs allow for very high solar absorption using orders of magnitude less active material than conventional solar cells.[20,21] The enhanced absorption comes from both reduced light reflection due to a graded refractive index near the surface and parallel-to-interface deflection of sunlight into slow-light modes with very long dwell times.[22] These effects rely on the wave nature of light and so cannot be captured using ordinary ray-tracing methods. The orders-of-magnitude reduction in the active layer thickness that photonic crystals enable has significant potential benefits in c-Si cells: aside from the reduction in materials costs due to the use of less material, there is also the possibility that less expensive, lower quality silicon could be used in the cell, as electrons and holes would not need to be transported as far. Thinner active layers also offer the potential of lightweight or flexible modules.

In this paper, we optically model a perovskite/c-Si tandem solar cell with a photonic crystal architecture consisting of a square-lattice array of inverted pyramids. The structure is based on the thin film single junction c-Si cell studied by Eyderman *et al.*[23] In that work, it was shown that a cell with

a)sfoster@physics.utoronto.ca

less than 10 μm (equivalent bulk thickness) of silicon and a 2.5 μm center-to-center pyramid spacing yields a maximum achievable photocurrent density (MAPD) of 42.5 mA/cm^2, out of a possible 43.5 mA/cm^2 in the wavelength range of 300–1100 nm. This is comparable to the absorption seen in the best available thick (150–300 μm) c-Si cells,[2] despite the use of an order of magnitude less silicon. In this work, we consider an extension of this design for a two-terminal tandem cell, with a 10 μm c-Si layer and a thin CH$_3$NH$_3$PbI$_3$ perovskite layer combined into a single, monolithically integrated stack. Although there have been several previous optical studies of perovskite/c-Si tandem cells,[24–26] most of these have made use of ray optics or transfer matrix methods of simulation, which makes them incapable of capturing photonic-crystal-based effects. Shi *et al.*[26] did make use of finite-difference time-domain (FDTD) techniques; however, they considered the case of a semi-infinite c-Si substrate, which ensures that all light entering the silicon subcell is absorbed. Here, we present the first optical simulation of a finite-sized perovskite/c-Si tandem cell based on a full solution to Maxwell's equations, using FDTD techniques. We find that as in the single-junction c-Si case, near-total solar absorption from 300 to 1100 nm can be achieved, with a combined (silicon + perovskite) MAPD of up to 41.5 mA/cm^2. To obtain a projected efficiency for the tandem cell, both subcells are characterized using a one-diode model. Using simulated MAPD values as input, the maximum power point (MPP) is found for each cell, and the thickness of the perovskite layer is adjusted until the current density at maximum power point (J_{MPP}) is the same for both subcells. After optimization of the cell geometry, a maximum projected efficiency of 30.6% is found, well beyond the current record efficiency for c-Si cells. It is noteworthy that this value is almost identical to what was found in a previous optical study of perovskite/c-Si tandem cells,[24] despite the fact that our design uses less than 1/10th the amount of silicon.

II. CELL STRUCTURE AND THEORETICAL MODEL

Figure 1 shows a diagram of the cell architecture studied in this work. The core of the design is a c-Si slab, height H, with a square-lattice array of inverted pyramids at the top of
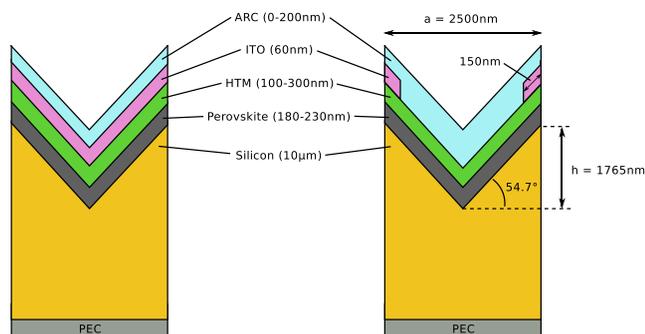

FIG. 1. Diagram of the cell architectures studied in this work. In the cell on the left, the ITO forms a thin (60 nm) conformal layer that covers the entire cell. In the cell on the right, the ITO forms a thin strip (60 nm thick, 150 nm wide) that runs around the outer edge of each pyramid.

the slab. Inverted pyramids can be readily formed on the surface of c-Si slabs through the use of alkaline etching,[27] which preferentially etches away silicon along the (111) crystal planes. A square-grid mask can be used to ensure that etched planes meet to form inverted pyramids. The characteristic angle of etching is $\alpha = 54.7°$, the angle between the (111) and (100) planes for silicon. As a result, the height of the pyramids is given by $h = a/(2 \tan(90 - \alpha))$, where a is the lattice constant of the array of pyramids. For this work, we consider a slab with $H = 10 \mu$m. We set $a = 2500$ nm, as this was previously found to be the optimal lattice constant for a 10 μm slab in the single-junction c-Si case.[23] This yields a pyramid height of $h = 1765$ nm.

From top to bottom, the other layers of the cell are an anti-reflective coating (ARC), ITO, a hole-transporting material (HTM), and CH$_3$NH$_3$PbI$_3$. These are layered conformally on top of the c-Si. Note that the conformal nature of the design means that the perovskite layer would likely not be able to be deposited using solution processing methods, and would instead have to be evaporated onto the substrate. However, there are examples of high-efficiency vapour-deposited perovskite cells in the literature.[28,29] The c-Si thin-film itself could be formed by removing it from a thick wafer, in a process such as epitaxial liftoff.[30,31] A potential experimental concern is that the thin-film c-Si could curl up after removal due to the surface stress created by the photonic crystal patterning. This issue, if prevalent, would have to be addressed before the design could see wide-scale application in the real world. One possibility is that the patterned regions could be filled in with a sacrificial material until the thin film is transferred to a suitable substrate.

The detailed nature of the cell materials and their optical properties is described below. We assume a very thin ($\sim$10 nm) TiO$_2$ tunnel junction is present between the perovskite and c-Si layers, as studied by Mailoa *et al.*[17] However, such a thin layer would have negligible optical effect and so is not included in our simulations. The thickness of the perovskite layer is varied in order to achieve current matching between the subcells; typical current-matching thickness was in the range of 190–220 nm. The thicknesses of the ARC and HTM layers were also varied to search for values that produced beneficial interference effects. In regards to the ITO, two cell architectures were considered: in the first case, the ITO is arranged in a "grid" pattern, similar to the cell studied by Albrecht *et al.*[16] Here, the ITO forms a thin strip, 150 nm wide and 60 nm thick, which runs around the outer edge of each pyramid. This is shown in the right of Figure 1. The motivation for this grid architecture was to study a case in which the ITO could still provide an electrical contact for the cell while covering a small surface area, so as to minimize parasitic absorption of light. However, such a design could be difficult to implement, so we also consider a more conventional design in which the ITO has a simple planar thin-film architecture, with a thickness of 60 nm. This is shown in the left of Figure 1. In addition to these layers, a metallic contact is present at the bottom of the cell, which we model as a perfect electrical conductor (PEC). Of course, in a real-world cell, some light would be lost due to parasitic absorption by the metal contact, which our model neglects. This would result in a slightly lower cell photocurrent

density than our projected MAPD. However, previous studies have found that parasitic absorption by metallic contacts is generally quite small, typically 0.3–0.8 mA/cm^2.[20,21,32]

All FDTD calculations were performed with the software package MEEP.[33] We use a standard FDTD calculation scheme in which the effect of a broadband pulse incident on the cell is modeled. Periodic boundary conditions are imposed in the x and y (lateral) directions, and perfectly matched layers (PMLs) are placed above and below the cell. Since there are multiple absorbing materials in the cell and we want to achieve current-matching between two of them, it is crucial to distinguish between absorption by the different layers. To do this, the field is recorded across a number of different surfaces, Fourier transformed, and then used to obtain the total flux across the surface in the frequency domain. The flux across a surface A_i is given by

$$S_i(\omega) = \int_{A_i} \Re[\mathbf{E}(\mathbf{r}, \omega) \times \mathbf{H}(\mathbf{r}, \omega)^*] \cdot \hat{n} \, dA, \qquad (1)$$

where $\mathbf{E}(\mathbf{r}, \omega)$ and $\mathbf{H}(\mathbf{r}, \omega)$ are the Fourier-transformed electric and magnetic fields, the superscript * represents the complex conjugate, and $\hat{n}$ is the unit normal vector for the surface A_i. The fraction of incident power absorbed in a given volume bounded by surfaces A_i (above) and A_j (below) is therefore given by

$$\alpha(\omega) = \frac{S_i(\omega) - S_j(\omega)}{S_{inc}(\omega)}. \qquad (2)$$

Here, $S_{inc}(\omega)$ is the incident flux as a function of angular frequency. This is obtained during a normalization run, in which the incident wave is sent through the same computational region with no materials present. It is given by the formula

$$S_{inc}(\omega) = \int_{A_0} \Re[\mathbf{E}_0(\mathbf{r}, \omega) \times \mathbf{H}_0(\mathbf{r}, \omega)^*] \cdot \hat{n} \, dA, \qquad (3)$$

where $\mathbf{E}_0$ and $\mathbf{H}_0$ are the (Fourier-transformed) electric and magnetic fields from the normalization run, and A_0 is a surface normal to the incident wave (placed at an arbitrary height). Note that Eq. (2) follows directly from Poynting's theorem, but relies on the fact that lateral periodic boundary conditions were imposed on the cell. This ensures that any power flowing out of the cell in the x or y direction is exactly matched by the power flowing in on the opposite side of the cell. As a result, only the surfaces bounding a given region above and below need to be considered.

Complex dielectric function data for silicon, perovskite, and ITO are taken from the literature.[34–36] In order to use these data in MEEP, the dielectric functions for each material must be fitted to a series of Lorentz terms. That is, the fitted dielectric function has the form

$$\varepsilon(\omega) = \varepsilon_\infty + \sum_j \frac{\Delta\varepsilon_j \omega_{p,j}^2}{\omega_{p,j}^2 - i\omega\gamma_j - \omega^2}, \qquad (4)$$

where ε_∞, $\Delta\varepsilon$, ω_p, and γ are parameters used to fit the experimental data. Fitting of the data was achieved through the use

of an open MATLAB program.[37] Plots of the fitted dielectric functions and parameter values for the fits are included in the Appendix.

The ARC and HTM layers are modeled as non-absorbing dielectric materials with a constant index of refraction. In the case of the ARC, we vary the refractive index between 1.25 and 1.55 over different calculations to search for the optimal value given our geometry. The HTM layer is assumed to have a refractive index of 1.75, which is close to the average refractive index of spiro-OMETAD,[24] a common hole-transporting material used in perovskite cells. For simplicity, we assume that the HTM layer is non-absorbing in this case, which neglects a small amount of parasitic absorption. However, HTM optimization for perovskite cells is an active research area,[38] and the potential exists for non-absorbing HTMs to be found in the future. Moreover, there has been recent progress on developing perovskite cells that are entirely HTM-free.[39] As our aim is to show what is ultimately possible with silicon/perovskite tandem cells, it is reasonable to discount HTM absorption in the present work.

Using the absorption spectrum, we calculate the MAPD for a given region with the formula

$$J_{MAPD} = \int_{\lambda_{min}}^{\lambda_{max}} \frac{e\lambda}{hc} I(\lambda)\alpha(\lambda) d\lambda, \qquad (5)$$

where e is the electric charge, λ is the vacuum wavelength, h is the Planck's constant, and c is the speed of light in a vacuum. $I(\lambda)$ is the standard AM1.5 solar spectrum, assumed to be collimated in a uniformly polarized beam normally incident on the cell. Polarization is taken to be along one of the two (equivalent) directions of periodicity. The integral is taken over the wavelength range of 300–1100 nm. The MAPD represents the highest possible photocurrent density that a cell could deliver given its optical characteristics. In most cases, MAPD provides a very close approximation for the short circuit current density, J_{sc}. The total available photocurrent density from 300 to 1100 nm, assuming all photons are absorbed and each photon generates one electron-hole pair, is 43.5 mA/cm^2.

We characterize the electrical properties of the subcells using a simple one-diode fitting function.[40] Under this model, the current density-voltage (J-V) curve for each subcell is given by the implicit formula

$$J = J_{MAPD} - J_0\left(\exp\left(\frac{V + JR_s}{nV_T}\right) - 1\right), \qquad (6)$$

where J_0 is the saturation current density, n is the diode ideality factor, and R_s is the series resistance. Shunt resistance[40] is very large for both cells, and so we neglect the contribution of shunt current to Eq. (6). The quantity $V_T = k_bT/e$ is the thermal voltage of the cell, where k_b is the Boltzmann's constant and T is the cell temperature, assumed to be 300 K. For silicon, model parameters are taken from Filipič et al.[24] For the perovskite subcell, the model parameters were obtained by fitting an experimental J-V curve from an 18% efficient cell in the literature.[41] This cell was chosen as it is both highly efficient and shows no current hysteresis. The values for these parameters are shown in Table I.

TABLE I. One-diode model parameters for the silicon and perovskite subcells.

Subcell	J_0 (mA/cm^2)	n	R_s ($\Omega \times$ cm^2)
Silicon	8.21×10^{-10}	1.170	0.070
Perovskite	1.46×10^{-11}	1.432	0.083

To calculate cell efficiency, MAPD values for both subcells are first obtained from FDTD calculations. Cell efficiency is highest when the power output of the cell is highest (called the maximum power point, or MPP). The current density and voltage at the maximum power point (J_{MPP} and V_{MPP}, respectively) can be calculated for a given cell geometry by differentiating the power (given by $J \cdot V$) with respect to voltage, and setting the result equal to zero. Solving this equation and Eq. (6) simultaneously yields J_{MPP} and V_{MPP} for each subcell. Because the two subcells are wired in series in a two-terminal configuration, current density is limited by the lower of the two subcell current densities. The total cell efficiency, assuming 1000 W/m^2 of incident radiation, is given by

$$\eta = \frac{min\left(J_{MPP}^{(Si)}, J_{MPP}^{(Per)}\right) \cdot \left(V_{MPP}^{(Si)} + V_{MPP}^{(Per)}\right)}{1000 \text{ W/m}^2}. \quad (7)$$

As a result of this current-limiting effect, the highest total efficiency is achieved when the two subcells have equal current at their maximum power point. This is achieved by varying the thickness of the perovskite layer, which trades off perovskite absorption against silicon absorption.

III. RESULTS AND DISCUSSION

A. Cell optimization

We start by optimizing the cell geometry in the case with a full ITO layer. For this section, we fix the refractive index of the ARC layer at 1.45, approximately the refractive index of glass. Section III B discusses the effect of varying the ARC index. Here, we vary the thickness of the ARC layer (h_{arc}) over the range of 0–200 nm, and the thickness of the HTM layer (h_{htm}) from 100 to 300 nm. It is computationally difficult to simultaneously vary the thickness of the perovskite layer (h_{per}) in order to search for a current-matching condition. Therefore, for these calculations, we simply set h_{per} equal to 200 nm, approximately the thickness that yields current-matching. Cell geometries were then evaluated based on the average MAPD of the subcells. Since photocurrent can be traded off between the subcells by simply adjusting the thickness of the perovskite layer, average

MAPD is a good indicator of cell performance. After this initial optimization, h_{per} is then varied to search for the exact thickness that gives current matching at MPP.

After performing this optimization, we find that the values for h_{arc} and h_{htm} which give the highest average MAPD are 150 nm and 60 nm, respectively. Fixing those values and varying h_{per} in 5 nm steps, we find that 205 nm is the actual value which yields the highest projected efficiency. For these geometrical parameters, we find that the total absorbed light (including ITO) amounts to 42.1 mA/cm^2 in current density, meaning 1.4 mA/cm^2 of potential current is lost to reflection. Absorption due to ITO is 1.1 mA/cm^2. MAPD is 20.6 mA/cm^2 for the silicon subcell and 20.4 mA/cm^2 for the perovskite subcell. Applying the one-diode model, we find that at MPP, the current density for both subcells is well matched at 19.5 mA/cm^2. The cell voltages at MPP are 0.632 V for the silicon subcell and 0.916 V for the perovskite subcell. This yields a projected efficiency of 12.3% for the silicon subcell and 17.9% for the perovskite subcell, giving a total projected efficiency of 30.2%. The performance characteristics for both subcells are summarized in Table II.

Figure 2(a) shows the absorption spectra of the different cell materials for this geometry. Total absorption is high (>80%) across the entire wavelength range, even close to 1100 nm where the intrinsic absorption of silicon is very weak. This demonstrates that significant light-trapping is taking place in the cell. ITO absorption is highest at short wavelengths, reaching roughly 40% at 300 nm. Figure 2(b) shows the current density at maximum power point (J_{MPP}) for both subcells as the perovskite layer thickness is varied. Also shown is the projected efficiency, calculated based on the lower of the two subcell current densities. The highest projected efficiency coincides with the crossover point of the current density curves, at $h_{per} = 205$ nm.

Next, to minimize parasitic absorption, we consider a cell with the ITO grid architecture. Again, the refractive index of the ARC layer is fixed at 1.45, and h_{arc} and h_{htm} are varied between 0–200 nm and 100–300 nm, respectively. For these calculations, h_{per} was set equal to 205 nm, and the geometries were again evaluated based on the average MAPD of the two subcells. After performing the calculations, the optimal values were found to be 30 nm for h_{arc} and 290 nm for h_{htm}. With these values fixed, h_{per} was then varied in 5 nm steps, and it was found that 205 nm was indeed the thickness that yielded the highest efficiency. With these geometrical parameters, we find ITO absorption is significantly reduced from the ITO layer case, going from 1.1 mA/cm^2 down to just 0.15 mA/cm^2. Some of this freed photocurrent simply passes through the cell, and so reflection losses increase slightly (1.9 mA/cm^2, versus 1.4 mA/cm^2 for the ITO layer geometry). However, the

TABLE II. Subcell performance characteristics for optimized cell geometries.

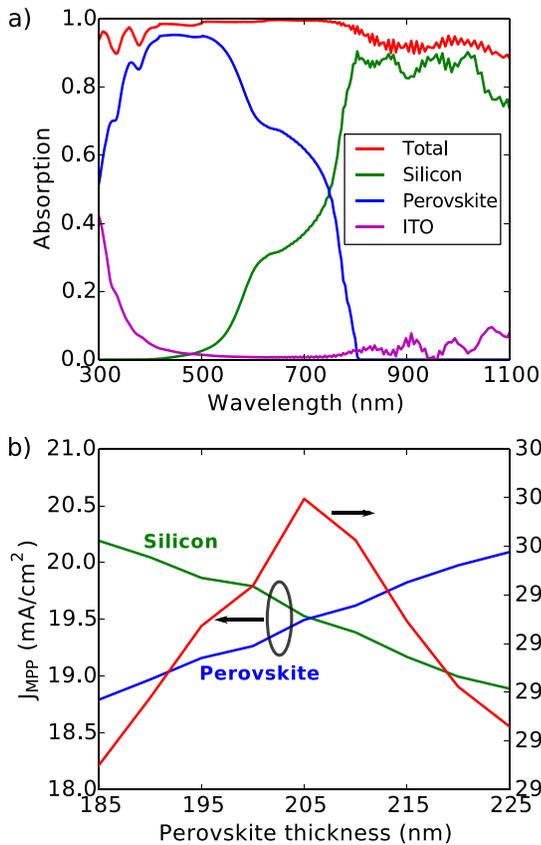|	Subcell	J_{MPP} (mA/cm^2)	V_{MPP} (V)	J_{sc} (mA/cm^2)	V_{oc} (V)	Fill factor	η (%)
ITO layer	Silicon	19.5	0.632	20.6	0.724	0.83	12.3
	Perovskite	19.5	0.916	20.4	1.035	0.85	17.9
ITO grid	Silicon	19.8	0.633	20.9	0.725	0.83	12.5
	Perovskite	19.7	0.917	20.6	1.036	0.85	18.1

FIG. 2. (a) Absorption spectra for the different materials in the cell, optimized ITO layer geometry. (b) Current density at maximum power point for the two subcells, as well as total projected cell efficiency, as a function of perovskite layer thickness.
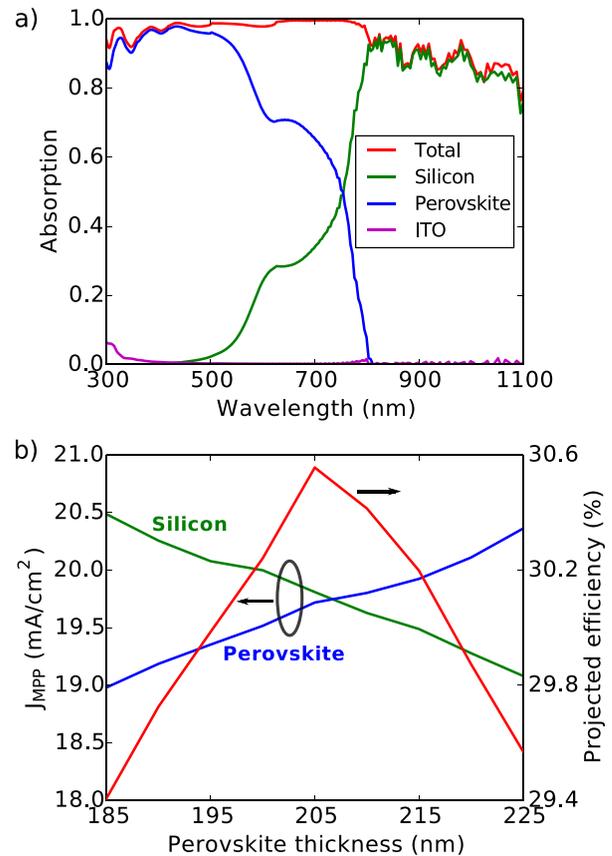

FIG. 3. (a) Absorption spectra for the different materials in the cell, optimized ITO grid geometry. (b) Current density at maximum power point for the two subcells, as well as total projected cell efficiency, as a function of perovskite layer thickness.

rest is absorbed by the two subcells, leading to an increase in MAPD. We find an MAPD of 20.9 mA/cm^2 for the silicon subcell and 20.6 mA/cm^2 for the perovskite subcell. Applying the one-diode model, we find that the current density at MPP is 19.8 mA/cm^2 for the silicon subcell and 19.7 mA/cm^2 for the perovskite subcell, very close to current-matching. The cell voltages at MPP are 0.633 V for the silicon subcell and 0.917 V for the perovskite subcell. This yields a projected efficiency of 12.5% for the silicon subcell and 18.1% for the perovskite subcell, giving a total projected efficiency of 30.6%. Cell performance characteristics are summarized in Table II.

Figure 3(a) shows the absorption spectra for the different materials in the cell with the optimized grid geometry. ITO absorption has been greatly reduced and is now below 5% absorption for all wavelengths. At shorter wavelengths, light that was previously absorbed by the ITO is now absorbed by the perovskite layer, and total absorption remains unchanged. However, at longer wavelengths, some of the freed light is not absorbed by the silicon subcell and simply passes through the cell, resulting in a decrease in total absorption. Figure 3(b) shows current density at MPP for the two subcells, along with the projected total efficiency, as a function of perovskite layer thickness.

Ultimately, since the perovskite subcell is capable of absorbing significantly more light than it does at present, this design is limited by the ability of silicon to absorb light at

long wavelengths. Near 1100 nm, we see that the silicon subcell is absorbing approximately 80% of incident light. This is well beyond what could be achieved in a 10 μm cell without light-trapping and is comparable to the long-wavelength absorption seen in 100 μm+ thick cells.[25] However, there is still room for improvement. Previous studies have shown that alternative structures optimized for light-trapping, such as slanted conical pores, can yield much stronger absorption than the inverted pyramids.[23] With such a design, long-wavelength absorption could likely be pushed above 90%.

The exact optimal thickness for silicon in a real-world cell depends on various trade-offs between material costs, electrical and optical performance, and manufacturing ease. From an optical perspective, we find that 10 μm is enough to achieve world-record absorption levels. Additional silicon would only yield small gains in absorption, with rapidly diminishing returns. On the other hand, previous work shows that reducing the silicon thickness below 10 μm leads to significantly reduced absorption.[23] This suggests that with an inverted pyramid photonic crystal design, 10 μm is close to the optimal thickness for silicon.

It is instructive to compare these results with those from other types of tandem cells, in particular, those based on amorphous silicon (a-Si). Like perovskite, a-Si has a high bandgap (1.7 eV), which makes it suitable to act as the top cell in a tandem design. The most commonly studied a-Si-based tandem is the "micromorph" cell, which uses microcrystalline silicon

(μc-Si) as a bottom cell material (bandgap of 1 eV).[42] A less common approach is to use c-Si for the bottom cell material.[43] A problem faced by both types of cell is that in order to ensure efficient charge collection, a-Si cells are limited to a thickness of a few hundred nanometers, which strongly limits the amount of light they can absorb. The best a-Si-based tandem cells typically have short-circuit current densities of roughly 13 mA/cm^2 and are current-limited by the a-Si subcell. This is far less than half of the total available photocurrent (21.75 mA/cm^2 for the 300–1100 nm spectral range), which an ideal tandem subcell would absorb. To mitigate this problem, some groups have made use of an intermediate reflecting layer (IRL) to boost absorption in the a-Si top cell.[44] However, this typically produces only modest gains. An additional problem is that a-Si cells tend to have relatively poor electrical characteristics, which limits the fill factor and open-circuit voltage of any a-Si-based tandem cell.

In contrast, for our design, both subcells absorb more than 20 mA/cm^2 of photocurrent. This is close to the maximum possible, making the introduction of an IRL unnecessary. In addition, current matching occurs when the perovskite thickness is at just 200 nm, well below the limits imposed by charge collection. Moreover, perovskite single-junction cells have excellent electrical properties, and it has already been demonstrated that they can be combined with c-Si to create tandem cells with high V_{oc} and fill factor.[16] It is clear that perovskite has far more potential as a top cell material in c-Si-based tandem cells than does a-Si, despite the fact that a-Si has a bandgap closer to the optimum.

B. Effect of ARC refractive index

Reducing reflection losses is essential to achieving high cell efficiencies. Although the inverted pyramids of our design provide some level of anti-reflection through their graded refractive index geometry, the ARC layer can provide additional anti-reflection. To examine the effect of changing the refractive index of the ARC on our design, we fix the thickness of the HTM and perovskite layers, and then vary the thickness of the ARC layer from 0 to 200 nm, and the refractive index of the ARC layer from 1.25 to 1.55. For the ITO layer geometry, we set $h_{htm} = 150$ nm and $h_{per} = 200$ nm, and for the grid geometry, we set $h_{htm} = 290$ nm and $h_{per} = 205$ nm. Note that for the grid geometry, even when $h_{arc} = 0$ nm, there is still a 60 nm thick layer of ARC material filling in the region where the ITO has been removed (see Figure 1). As before, we evaluate cells based on the average MAPD of the subcells.

Figure 4 shows our results for the ITO layer geometry and ITO grid geometry. Both graphs show the average MAPD of the subcells as a function of ARC layer thickness, for the four different refractive index values considered. For the ITO layer geometry, average MAPD first increases with ARC thickness (with peaks at 60 nm and 100 nm) and then decreases beyond $h_{arc} = 100$ nm. For the grid geometry, we see a small peak in average MAPD at $h_{arc} = 30$ nm, and then a decrease with higher values of h$_{arc.}$ Both geometries show a similar pattern with respect to the refractive index: when the ARC is very thin, refractive index matters very little.
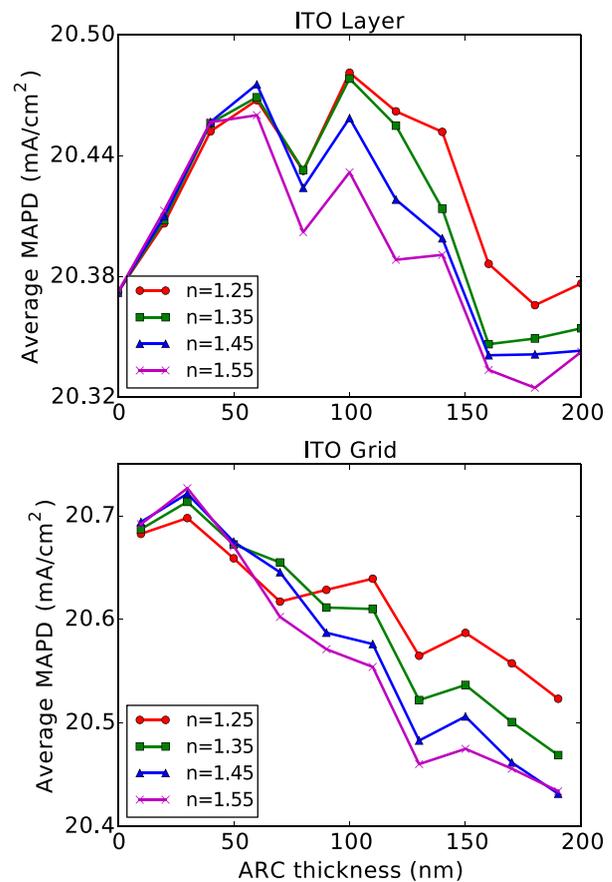

FIG. 4. Average MAPD of the two subcells as a function of ARC layer thickness for ITO layer architecture (upper graph) and ITO grid architecture (lower graph). Four different values for the refractive index of the ARC are considered, from 1.25 to 1.55.

When the ARC is thicker, however, lower refractive index values tend to give slightly higher average MAPDs.

Overall, changing the thickness and refractive index of the ARC has a very little effect (the vertical scales for the graphs of Figure 4 are small, especially in the case of the ITO layer geometry). The most significant trend we see (for the case of the grid geometry) is that average MAPD decreases by ~0.3 mA/cm^2 as h_{arc} is increased from 0 to 200 nm. Meanwhile, for both geometries, varying the refractive index from 1.25 to 1.55 produces shifts in the average MAPD of only 0.1 mA/cm^2 or less. These results suggest that for our design, ARC provides minimal additional anti-reflection beyond that provided by the inverted pyramids themselves.

IV. CONCLUSION

Using finite-difference time-domain simulations, we have demonstrated the effectiveness of an inverted pyramid photonic crystal-based design for silicon/perovskite tandem cells. We have shown that, despite the use of less than 10 μm of silicon, the design allows for near-total absorption of the solar spectrum from 300 to 1100 nm thanks to strong light-trapping effects. Two cell architectures were considered: one in which the ITO formed a thin-film conformal layer, and the other in which the ITO formed a thin "grid," with strips running around the outer edges of the inverted pyramids. For

the ITO layer architecture, after geometric optimization, we found that the active layers produced a combined MAPD of 41.0 mA/cm^2. For the optimized grid geometry, the combined MAPD was 41.5 mA/cm^2. These figures are comparable to the short-circuit current density of state-of-the-art single-junction c-Si cells, which typically use 150 μm of silicon or more. To obtain projected efficiencies for our design, we characterized the electrical properties of the silicon and perovskite subcells using a one-diode model. After varying the thickness of the perovskite layer to achieve current-matching between the subcells, we found a projected efficiency of 30.2% for the ITO layer architecture, and 30.6% for the grid architecture, with a projected V_{oc} of 1.76 V. These efficiencies are both well beyond the record efficiency for single-junction c-Si cells. An investigation of the effect of the ARC layer found that changing ARC thickness and refractive index had a relatively small effect on cell performance.

Silicon/perovskite tandem cells represent a promising new direction for solar cell research. However, most work to date in the field has focused on traditional, bulky silicon cells. Our work demonstrates that with proper light-trapping through the use of inverted pyramids, thin-film silicon cells of thickness 10 μm or less are a viable option for pairing with perovskite in tandem cells. Indeed, we find that thicknesses beyond 10 μm provide little benefit from an optical perspective. Moreover, our design is amenable to mass manufacture through the use of wet-etching. We hope that our work encourages further study of thin-film photonic crystal-based silicon/perovskite tandem solar cells, with the potential to achieve world-record-breaking efficiencies.

ACKNOWLEDGMENTS

APPENDIX: DIELECTRIC FUNCTION FITTING

Since MEEP cannot directly make use of tabulated dielectric function data, dielectric functions for dispersive materials must be modelled as a series of Lorentz oscillators (with the functional form given in Eq. (4)). In the case of ITO, it was found that the dielectric function could be well-approximated over the entire wavelength range of interest (300–1100 nm) using a single fit with four Lorentz terms. However, for silicon and perovskite, it was found that it was impossible to approximate the dielectric function using a single fit, even with a large number of Lorentz terms. For these materials, multiple fits were obtained, each valid over a different wavelength range. It is actually possible to

TABLE III. Best fit values for dielectric function models.

Material	ε_∞	$\Delta\varepsilon$	ω_p (μm^{-1})	γ (μm^{-1})
Silicon (300–380 nm)	6.547	6.334	21.463	0.578
		1.315	17.291	0.174
		3.062	18.661	0.512
		−0.200	16.481	0.072
Silicon (370–1100 nm)	1.000	7.886	22.312	0.010
		−0.039	7.502	1.002
		1.156	17.637	0.000
		1.651	17.115	0.144
Perovskite (300–800 nm)	3.514	−0.200	10.534	0.334
		1.673	17.582	0.855
		1.076	12.840	1.033
		−0.084	7.750	0.119
		−0.011	8.092	0.060
Perovskite (800–1100 nm)	4.956	0.141	8.395	0.000
ITO (300–1100 nm)	2.810	−0.133	20.928	1.196
		−0.058	16.476	2.427
		1.177	26.144	0.596
		9.999	2.665	0.011

characterize the dielectric function of silicon over the entire 300–1100 nm wavelength range using a single fit; however, this requires using a "modified" Lorentz term as described by Deinega and John,[45] and MEEP is not capable of implementing such modified Lorentz terms (other software packages, such as EMTL, do have this capability).
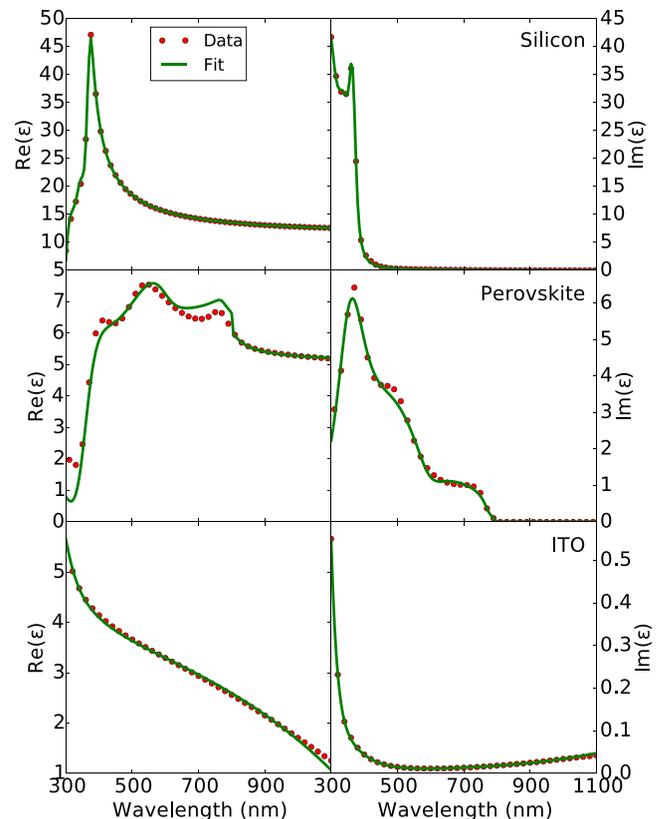

FIG. 5. Real and imaginary components of the dielectric function for silicon (upper graph), perovskite (middle graph), and ITO (lower graph): comparison of experimental data (circles) with fitted functions (lines).

For silicon, it was found that the dielectric function could be approximated closely from 300 to 380 nm with four Lorentz terms, and from 370 to 1100 nm with another four Lorentz terms. In the case of perovskite, it was found that five Lorentz terms were able to fit the data closely from 300 to 800 nm, and a single Lorentz term was adequate for the range 800–1100 nm. The use of multiple fits meant that for each cell geometry considered, multiple calculations had to be run, with a different fit applied for each calculation. Data were then taken from the valid spectral region of each calculation and combined to form full transmission, reflection, and absorption spectra.

The parameter values for all fits are shown in Table III. Note that ω_p represents an angular frequency and has units of μm^{-1} (with the speed of light set to unity). The units of γ are also μm^{-1}. Some works use a slightly different version of Eq. (4) in which a factor of 2 is taken out of the definition of γ, which should be noted when importing fitted dielectric functions into different FDTD software packages. Plots of the fitted dielectric functions, along with experimental data, are shown in Fig. 5.

[1]See http://www.itrpv.net/Reports/Downloads/2014/ for International Technology Roadmap for Photovoltaics.

[2]K. Masuko, M. Shigematsu, T. Hashiguchi, D. Fujishima, M. Kai, N. Yoshimura, T. Yamaguchi, Y. Ichihashi, T. Yamanishi, T. Takahama, M. Taguchi, E. Maruyama, S. Okamoto, T. Mishima, N. Matsubara, T. Yamanishi, T. Takahama, M. Taguchi, E. Maruyama, and S. Okamoto, "Achievement of more than 25% conversion efficiency with crystalline silicon heterojunction solar cell," IEEE J. Photovoltaics **4**, 1433–1435 (2014).

[3]A. Richter, M. Hermle, and S. W. Glunz, "Reassessment of the limiting efficiency for crystalline silicon solar cells," IEEE J. Photovoltaics **3**, 1184–1191 (2013).

[4]K. Tanabe, "A review of ultrahigh efficiency III-V semiconductor compound solar cells: Multijunction tandem, lower dimensional, photonic up/down conversion and plasmonic nanometallic structures," Energies **2**, 504–530 (2009).

[5]J. You, L. Dou, K. Yoshimura, T. Kato, K. Ohya, T. Moriarty, K. Emery, C.-C. Chen, J. Gao, G. Li, and Y. Yang, "A polymer tandem solar cell with 10.6% power conversion efficiency," Nat. Commun. **4**, 1446 (2013).

[6]C.-C. Chen, W.-H. Chang, K. Yoshimura, K. Ohya, J. You, J. Gao, Z. Hong, and Y. Yang, "An efficient triple-junction polymer solar cell having a power conversion efficiency exceeding 11%," Adv. Mater. **26**, 5670 (2014).

[7]T. Kinoshita, J. T. Dy, S. Uchida, T. Kubo, and H. Segawa, "Wideband dye-sensitized solar cells employing a phosphine-coordinated ruthenium sensitizer," Nat. Photonics **7**, 535 (2013).

[8]X. Wang, G. I. Koleilat, J. Tang, H. Liu, I. J. Kramer, R. Debnath, L. Brzozowski, D. A. R. Barkhouse, L. Levina, S. Hoogland, and E. H. Sargent, "Tandem colloidal quantum dot solar cells employing a graded recombination layer," Nat. Photonics **5**, 480–484 (2011).

[9]T. Kim, Y. Gao, H. Hu, B. Yan, Z. Ning, L. K. Jagadamma, K. Zhao, A. R. Kirmani, J. Eid, M. M. Adachi, E. H. Sargent, P. M. Beaujuge, and A. Amassian, "Hybrid tandem solar cells with depleted-heterojunction quantum dot and polymer bulk heterojunction subcells," Nano Energy **17**, 196–205 (2015).

[10]H. Tan, A. Furlan, W. Li, K. Arapov, R. Santbergen, M. M. Wienk, M. Zeman, A. H. M. Smets, and R. A. J. Janssen, "Highly efficient hybrid polymer and amorphous silicon multijunction solar cells with effective optical management," Adv. Mater. **28**, 2170–2177 (2016).

[11]M. Sessolo and H. J. Bolink, "Perovskite solar cells join the major league," Science **350**, 917 (2015).

[12]Dyesol press release, EPFL Achieves 21% Efficiency for Perovskites, December 8 2015.

[13]W. E. I. Sha, X. Ren, L. Chen, and W. C. H. Choy, "The efficiency limit of $CH_3NH_3PbI_3$ perovskite solar cells," Appl. Phys. Lett. **106**, 221104 (2015).

[14]A. Shah, P. Torres, R. Tscharner, N. Wyrsch, and H. Keppner, "Photovoltaic technology: The case for thin-film solar cells," Science **285**, 692–698 (1999).

[15]D. P. McMeekin, G. Sadoughi, W. Rehman, G. E. Eperon, M. Saliba, M. T. Hrantner, A. Haghighirad, N. Sakai, L. Korte, B. Rech, M. B. Johnston, L. M. Herz, and H. J. Snaith, "A mixed-cation lead mixed-halide perovskite absorber for tandem solar cells," Science **351**, 151–155 (2016).

[16]S. Albrecht, M. Saliba, J. P. C. Baena, F. Lang, L. Kegelmann, M. Mews, L. Steier, A. Abate, J. Rappich, L. Korte, R. Schlatmann, M. K. Nazeeruddin, A. Hagfeldt, M. Gratzel, and B. Recha, "Monolithic perovskite/silicon-heterojunction tandem solar cells processed at low temperature," Energy Environ. Sci. **9**, 81 (2016).

[17]J. P. Mailoa, C. D. Bailie, E. C. Johlin, E. T. Hoke, A. J. Akey, W. H. Nguyen, M. D. McGehee, and T. Buonassisi, "A 2-terminal perovskite/silicon multijunction solar cell enabled by a silicon tunnel junction," Appl. Phys. Lett. **106**, 121105 (2015).

[18]S. John, "Strong localization of photons in certain disordered dielectric superlattices," Phys. Rev. Lett. **58**, 2486 (1987).

[19]E. Yablonovitch, "Inhibited spontaneous emission in solid-state physics and electronics," Phys. Rev. Lett. **58**, 2059 (1987).

[20]S. Eyderman, S. John, and A. Deinega, "Solar light trapping in slanted conical-pore photonic crystals: Beyond statistical ray trapping," J. Appl. Phys. **113**, 154315 (2013).

[21]S. Eyderman, A. Deinega, and S. John, "Near perfect solar absorption in ultra-thin-film GaAs photonic crystals," J. Mater. Chem. A **2**, 761–769 (2014).

[22]A. Chutinan and S. John, "Light trapping and absorption optimization in certain thin–film photonic crystal architectures," Phys. Rev. A **78**, 023825 (2008).

[23]S. Eyderman, S. John, M. Hafez, S. S. Al-Ameer, T. S. Al-Harby, Y. Al-Hadeethi, and D. M. Bouwes, "Light-trapping optimization in wet-etched silicon photonic crystal solar cells," J. Appl. Phys. **118**, 023103 (2015).

[24]M. Filipič, P. Lper, B. Niesen, S. De Wolf, J. Krč, C. Ballif, and M. Topič, "$CH_3NH_3PbI_3$ perovskite/silicon tandem solar cells: Characterization based optical simulations," Opt. Express **23**, A263–A278 (2015).

[25]B. W. Schneider, N. N. Lal, S. Baker-Finch, and T. P. White, "Pyramidal surface textures for light trapping and antireflection in perovskite-on-silicon tandem solar cells," Opt. Express **22**(S6), A1422–A1430 (2014).

[26]D. Shi, Y. Zeng, and W. Shen, "Perovskite/c-Si tandem solar cell with inverted nanopyramids: Realizing high efficiency by controllable light trapping," Sci. Rep. **5**, 16504 (2015).

[27]H.-H. Lin and W.-H. Chen, "Improvement of polycrystalline silicon wafer solar cell efficiency by forming nanoscale pyramids on wafer surface using a self-mask etching technique," J. Vac. Sci. Technol., B **31**, 031401 (2013).

[28]M. Liu, M. B. Johnston, and H. J. Snaith, "Efficient planar heterojunction perovskite solar cells by vapour deposition," Nature **501**, 395–398 (2013).

[29]C.-W. Chen, H.-W. Kang, S.-Y. Hsiao, P.-F. Yang, K.-M. Chiang, and H.-W. Lin, "Efficient and uniform planar-type perovskite solar cells by simple sequential vacuum deposition," Adv. Mater. **26**, 6647–6652 (2014).

[30]C.-W. Cheng, K.-T. Shiu, N. Li, S.-J. Han, L. Shi, and D. K. Sadana, "Epitaxial lift-off process for gallium arsenide substrate reuse and flexible electronics," Nat. Commun. **4**, 1577 (2013).

[31]S. Kajari-Schrder, J. Ksewieter, J. Hensen, and R. Brendel, "Lift-off of free-standing layers in the kerfless porous silicon process," Energy Procedia **38**, 919–925 (2013).

[32]Z. C. Holman, M. Filipic, B. Lipovsek, S. De Wolf, F. Smole, M. Topic, and C. Ballif, "Parasitic absorption in the rear reflector of a silicon solar cell: Simulation and measurement of the sub-bandgap reflectance for common dielectric/metal reflectors," Sol. Energy Mater. Sol. Cells **120**, 426–430 (2014).

[33]A. F. Oskooi, D. Roundy, M. Ibanescu, P. Bermel, J. D. Joannopoulos, and S. G. Johnson, "MEEP: A flexible free-software package for electromagnetic simulations by the FDTD method," Comput. Phys. Commun. **181**, 687–702 (2010).

[34]E. D. Palik, *Handbook of Optical Constants of Solids* (Academic Press, Boston, 1985).

[35]T. A. F. Knig, P. A. Ledin, J. Kerszulis, M. A. Mahmoud, M. A. El-Sayed, J. R. Reynolds, and V. V. Tsukruk, "Electrically tunable plasmonic behavior of nanocube-polymer nanomaterials induced by a redox-active electrochromic polymer," ACS Nano **8**, 6182–6192 (2014).

[36]P. Lper, M. Stuckelberger, B. Niesen, J. Werner, M. Filipic, S.-J. Moon, J.-H. Yum, M. Topic, S. De Wolf, and C. Ballif, "Complex refractive index spectra of $CH_3NH_3PbI_3$ perovskite thin films determined by

spectroscopic ellipsometry and spectrophotometry," J. Phys. Chem. Lett. **6**, 66–71 (2015).

[37]See http://fdtd.kintechlab.com/en/fitting for fitting of dielectric function.

[38]S. Ameen, M. A. Rub, S. A. Kosa, K. A. Alamry, M. S. Akhtar, H.-S. Shin, H.-K. Seo, A. M. Asiri, and M. K. Nazeeruddin, "Perovskite solar cells: Influence of hole transporting materials on power conversion efficiency," ChemSusChem **9**, 10–27 (2016).

[39]L. Etgar, "Hole-transport material-free perovskite-based solar cells," MRS Bull. **40**, 674–680 (2015).

[40]J. L. Gray, "The physics of the solar cell," in *Handbook of Photovoltaic Science and Engineering*, edited by A. Luque and S. Hegedus (John Wiley and Sons, 2011).

[41]C.-G. Wu, C.-H. Chiang, Z.-L. Tseng, Md. K. Nazeeruddin, A. Hagfeldt, and M. Gratzel, "High efficiency stable inverted perovskite

solar cells without current hysteresis," Energy Environ. Sci. **8**, 2725–2733 (2015).

[42]H. Keppner, J. Meier, P. Torres, D. Fischer, and A. Shah, "Microcrystalline silicon and micromorph tandem solar cells," Appl. Phys. A **69**, 169–177 (1999).

[43]G. Li, H. Li, J. Y. L. Ho, M. Wong, and H. S. Kwok, "Nanopyramid structure for ultrathin c-Si tandem solar cells," Nano Lett. **14**, 2563–2568 (2014).

[44]M. Boccard, M. Despeisse, J. Escarre, X. Niquille, G. Bugnon, S. Hanni, M. Bonnet-Eymard, F. Meillaud, and C. Ballif, "High-stable-efficiency tandem thin-film silicon solar cell with low-refractive-index silicon-oxide interlayer," IEEE J. Photovoltaics **4**, 1368–1373 (2014).

[45]A. Deinega and S. John, "Effective optical response of silicon to sunlight in the finite-difference time-domain method," Opt. Lett. **37**, 112–114 (2012).